Journal of Nanophotonics

SPIEDigitalLibrary.org/jnp

Fabrication and realistic modeling of three-dimensional metal-dielectric composites

Mark D. Thoreson
Jieran Fang
Alexander V. Kildishev
Ludmila J. Prokopeva
Piotr Nyga
Uday K. Chettiar
Vladimir M. Shalaev
Vladimir P. Drachev

SPIE

Fabrication and realistic modeling of three-dimensional metal-dielectric composites

Mark D. Thoreson,[a,b] Jieran Fang,[a] Alexander V. Kildishev,[a] Ludmila J. Prokopeva,[c] Piotr Nyga,[d] Uday K. Chettiar,[e] Vladimir M. Shalaev,[a] and Vladimir P. Drachev[a]

[a] Purdue University, Birck Nanotechnology Center and School of Electrical and Computer Engineering, 1205 West State Street, West Lafayette, Indiana 47907
vdrachev@purdue.edu

[b] Friedrich-Alexander-Universität, Erlangen Graduate School for Advanced Optical Technologies (SAOT), Erlangen-Nürnberg, Erlangen, 91052, Germany

[c] Institute for Computational Technologies, Russian Academy of Sciences, Novosibirsk, 630090, Russia

[d] Institute of Optoelectronics, Military University of Technology, 00-908 Warsaw 49, Poland

[e] University of Pennsylvania, Department of Electrical and Systems Engineering, Philadelphia, Pennsylvania 19104

Abstract. Historically, the methods used to describe the electromagnetic response of random, three-dimensional (3D), metal-dielectric composites (MDCs) have been limited to approximations such as effective-medium theories that employ easily-obtained, macroscopic parameters. Full-wave numerical simulations such as finite-difference time domain (FDTD) calculations are difficult for random MDCs due to the fact that the nanoscale geometry of a random composite is generally difficult to ascertain after fabrication. We have developed a fabrication method for creating semicontinuous metal films with arbitrary thicknesses and a modeling technique for such films using realistic geometries. We extended our two-dimensional simulation method to obtain realistic geometries of 3D MDC samples, and we obtained the detailed near- and far-field electromagnetic responses of such composites using FDTD calculations. Our simulation results agree quantitatively well with the experimentally measured far-field spectra of the real samples.
 [DOI: 10.1117/1.3590208]

Keywords: metal-dielectric films; three-dimensional composites; finite-difference time domain modeling; cermets.

Paper 11007SSR received Jan. 17, 2011; revised manuscript received Apr. 14, 2011; accepted for publication Apr. 15, 2011; published online May 23, 2011.

1 Introduction

There is a demand for three-dimensional (3D), randomly arranged, metal-dielectric composites in a number of applications such as surface-enhanced processes, nonlinear optical devices, metamaterials, and obscurants, among others. Typically, metal films near the percolation threshold can be deposited only at a certain metal mass thickness, which is about 5 to 7 nm for gold and 9 to 11 nm for silver on glass or silicon. Perhaps more challenging is the full-wave simulation of such random films. Randomly arranged composites of nanoscale metal and dielectric elements, sometimes known as metal-dielectric composites (MDCs) or cermets,[1–4] are useful in a wide variety of electromagnetic and optical processes. These composites are therefore a topic of research for scientists interested in fundamental light-matter interactions as well as for engineers attempting to exploit the properties of MDCs in new applications. Random MDC films can

1934-2608/2011/$25.00 © 2011 SPIE

exhibit self-affine or fractal morphologies[5,6] that consist of nanometer-sized metallic particles formed by clusters and elongated islands of metal in a dielectric host. These metal nanostructures resonate in a broad spectral range extending from the UV into the mid-IR,[7,8] and random MDCs have rather unusual optical and electrical properties that are significantly different from their constituents. In particular, MDCs show quite interesting properties near the percolation threshold, which is defined as the metal volume fraction [or metal surface coverage for two-dimensional (2D) films] at which the electrical conductivity of the system undergoes a transition from being dielectric in nature to metallic in nature. Due to their resonant response and fractal morphology, random metal-dielectric composite systems can localize electromagnetic energy in nanometer-sized regions called hot spots, and they can also produce large near-field enhancement of electric and magnetic fields in the visible and infrared spectral ranges.[9–12] Materials placed in the near-field region of a random MDC film experience dramatically enhanced optical responses; this feature is employed in applications such as highly sensitive surface-enhanced Raman spectroscopies[13–17] and surface-enhanced infrared absorption spectroscopies,[18–21] enhanced solar cell efficiencies,[22,23] or for developing novel optical elements such as optical filters with transparency windows that can be controlled by local photomodification in the composites.[24,25]

Due to their varying applications, MDCs have been a topic of research for many decades. However, accurate simulations of random metal-dielectric systems are still challenging for several reasons, not the least of which is the complexity of the problem. Simulations of complex metal-dielectric structures have been largely focused in one of two categories. For periodic structures or those with a known geometry, researchers numerically studied the system using finite-element methods, finite-difference methods, or even analytical methods when possible. The other category for numerical simulations deals with modeling the properties of the random system using macroscopic parameters that are relatively easy to obtain. An example of this is the use of volume filling fractions and constituent permittivities in Bruggeman's effective medium theory (EMT)[26] and the Maxwell–Garnett theory (and modifications thereof).[27] Unfortunately, neither of these techniques is sufficiently accurate for random metal-dielectric structures with strongly interacting metallic elements. This is due to the fact that simple models such as EMT do not take into account metal-particle interactions and therefore fail to properly predict important aspects of the film response, such as the strong and broadband absorptance that is observed experimentally.[28]

In our case, the advantages of using the finite-difference time-domain (FDTD) method[29] are two-fold. First, we have developed a parallel version of the 3D FDTD solver that exploits the decomposition of the simulation domain, thus providing an almost linear speed-up increase as the number of sub-domains (and therefore the number of processors computing in parallel) increases.[30,31] In contrast with our parallel time-domain solver, the computer cluster solutions for the given large simulation domains appear less advantageous for frequency-domain solvers, even if a scalable, commercial, finite-element software package that we typically employ for frequency-domain simulations is used. This is because the dimensions of the system matrix in our case are very large, and there is no way to treat the problem in the "single-node per single frequency" regime, as the matrix usually does not fit into the single-node memory.

Second, we perform full 3D FDTD simulations that probe the transient response with a short, modulated Gaussian pulse because by doing so we reduce the overall time necessary for our numerical spectroscopic studies. As the transient response of a short pulse is broadband, we obtain the broadband spectral results from a single FDTD simulation instead of running a number of frequency-domain simulations to cover the needed wavelength range. By using the pulse excitation on top of the simulation domain decomposition, we additionally drastically reduce the overall simulation time. The speed-up of this approach is consistent with known analyses (see, for example Ref. 32). The equivalence of the steady-state and transient solutions for our general dispersive material models has been validated previously for the main numerical implementations of optical dispersion in the FDTD method, including the auxiliary differential equations approach and the typical variations of the second-order accurate recursive convolution schemes.[33]

In order to simulate the broadband responses properly, numerical methods require a known geometry. Unfortunately, the exact geometries of random metal-dielectric films are essentially impossible to predict before fabrication and nontrivial to obtain after fabrication, particularly for relatively thick MDC films composed of many layers of metal inclusions in a dielectric host. The randomness of the metal nanoparticle sizes and shapes is a significant hurdle to using the FDTD method for the calculations since the method requires a known geometry. In MDCs, the locations, orientations, sizes, and other properties of the nanoscale elements in the sample are not known, and the prediction of these properties using growth modeling, for example, is also a challenging topic of research.

In a previous paper,[30] we employed a method for obtaining realistic geometries of 2D (single-metal-layer) films and then simulating these geometries using the FDTD technique. In this work, we describe a flexible fabrication technique for making 3D MDC samples with controllable metal filling fractions and particle sizes. We then extend our 2D simulation method to these inherently 3D films, describing in detail how we obtain realistic geometries for use in simulating 3D MDC samples. We use a hybrid of real sample data and simulated geometries in order to calculate the electromagnetic response of 3D MDCs composed of thick stacks of random metal and dielectric films deposited on a dielectric substrate. Finally, we compare our simulation results to experimentally measured spectra and provide an outlook for these techniques for other applications of MDCs.

2 Methods

2.1 2D Footprinting Method and Simulations

The 2D footprint method we developed and described previously[30] is very effective for single-metal-layer films that can be modeled using a two-dimensional geometry. The principle of the method is to obtain a number of scanning electron microscopy (SEM) images of a fabricated sample and then convert these images or portions of them into geometries that can be fed into the FDTD solver. Herein we refer to this method as "footprinting" for convenience. The method begins with imaging a MDC film using a low-kV, field-emission SEM at various magnifications in order to obtain suitable images for further processing. The mass average thickness is known from the sample fabrication parameters, and the far-field spectral responses of the film are measured with a commercial UV/vis/near-infrared (NIR) spectrophotometer. We then convert the grayscale SEM images into binary (black and white) images in which the black areas represent the dielectric material and the white areas represent metal. We employ a thresholding process in order to find the edges of the metal regions, and this process is only partially automated. For each sample and each SEM image, manual adjustments of the thresholding function are necessary to ensure accurate selection of the metal and dielectric regions (see Fig. 1).

Once we have a binary image of the MDC film, we then section the image into frames roughly 100 × 100 pixels in size and create a thin film from the image by assuming a uniform

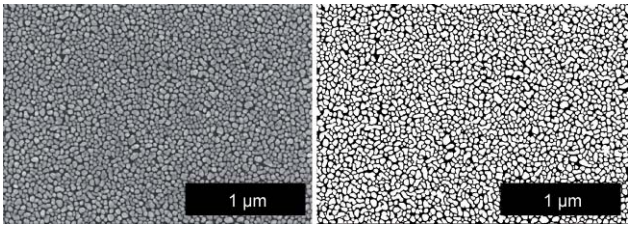

Fig. 1 Original SEM image of a fabricated film (left) is converted into a binary black/white image suitable for FDTD analysis (right). More than 20 sections of the black/white image are used as different realizations of the film nanostructure. The overall film response is then obtained by averaging the responses from each realization. This film shows a silver coverage of 66.8%.

thickness for the metal regions. Consistent with our AFM data (not shown), for 2D films we have used a thickness of 20 nm for the metal regions with vertical sidewalls. We then feed each frame successively into the FDTD solver to calculate the full-wave electromagnetic response. In our simulations, we used a Drude model matched to published data[34] for the permittivity of the silver constituent material, and we used a constant refractive index of 1.445 for the silicon dioxide constituent. It is also important to note that the dielectric function of plasmonic metals can differ from the bulk values.[35,36]

The edge of each pixel in the processed image represents from 1 to about 10 nm in real length, depending on the magnification of the initial SEM image. We typically use high-magnification images (50 to 100 K or higher), giving us reasonable detail in the image without requiring extensive computational time. The response from an individual section of the SEM image is not representative of the whole film, due to edge effects from the truncation process or nonuniformities of the film nanostructure observed under very high magnification. Therefore, we use many frames from the same SEM image or even multiple SEM images in order to build up a macroscopic average response for the entire sample. The overall far-field spectra of the sample are computed by averaging the spectra from a number of realizations created from one or more SEM images of the sample. In our work, we have found that approximately 20 iterations or geometry realizations are necessary to replicate the experimentally observed spectral responses of 2D (Ref. 30) or 3D films. The initial step of the footprinting process is shown in Fig. 1.

2.2 3D Composite Film Fabrication

In this section, we describe in detail a method to create complex, random, 3D MDCs using a multistep layering technique. Our method is qualitatively similar to that described above for 2D films, but in this case we repeat the sequential depositions of metal and dielectric layers in order to produce a truly 3D composite. By adjusting the mass average thickness of each metal layer, we can tailor the metal particle sizes with relative ease. By adjusting the mass average thickness of the dielectric layers, we can adjust the average spacing between adjacent metal particles or metal layers. Overall, these controllable parameters can be used to create a wide range of MDC structures, from complete random and small metal inclusions in a dielectric host, to a structure with uniform metal and dielectric layers, and many other designs. This technique is very flexible and relatively easy to tailor for any number of applications.

We fabricated a number of 3D MDC samples for our experiments using electron-beam evaporation, a physical vapor deposition technique. The initial substrates of either borosilicate glass or silicon wafers were first cleaned with an acidic solution (piranha solution, H_2O_2:$2H_2SO_4$) for 20 min, after which the substrates were thoroughly rinsed in nanograde water* (Ref. 37) followed by multiple rinses in acetone, methanol, and isopropanol. The clean substrates were then placed in an electron-beam vacuum evaporation chamber. The initial pressure inside the chamber was about 10^{-6} Torr. We first coated the samples with about 10 nm (mass average thickness) of silicon dioxide to obtain an appropriately adhesive surface for subsequent metal deposition. We first deposited a thin ($\sim$10 nm) layer of silica onto the substrate. We then deposited alternating layers of silver (3 to 12 nm deposited at 0.05 nm/s) and silica (1.3 to 6.3 nm, 0.1 nm/s), being careful to maintain the same deposition rates in each respective layer. Between each deposited layer, we allowed the evaporation system to cool and the deposited material to diffuse somewhat across the sample surface. Silver grows on glass and silicon in the Volmer–Weber growth mode,[38] so the ultrathin metal layers actually produce small, isolated, spheroidal particles of silver rather than a uniformly smooth layer. Silica, on the other hand, tends to wet the surface of the metal (and the previously-deposited silica regions), producing a relatively uniform coverage even for rather small mass average layer thicknesses. Hence, we

*The ultrapure (or nano-grade) water at the Birck Nanotechnology Center is incredibly pure. This water is below the measurement limits of 15 parts per trillion of boron, the most likely ionic impurity in the water. This water also contains less than 225 parts per trillion of total oxidizable carbon (TOC) and less than 1 part per billion of dissolved oxygen.

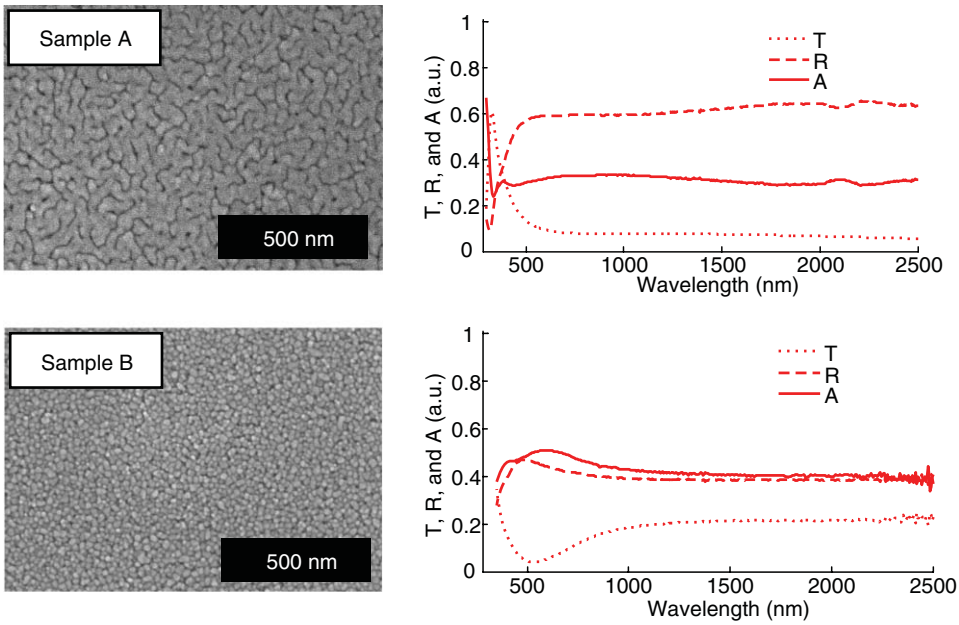

Fig. 2 Representative SEM images and measured far-field reflectance (R), transmittance (T) and absorptance (A) spectra of 3D composite films (Samples A and B) made of silver and silica. The samples are designed to have the same metal volume fraction and the same total thickness.

find that the silver nanoparticles are coated in silica, allowing for the next silver nanoparticles to form primarily on an amorphous silica surface and again grow as spheroidal particles. Repeating the alternating metal and dielectric layers then gives us the ability to create truly random, 3D composites with adjustable metal particle sizes at any film thickness.

It is important to note that because silver grows on glass or silicon in the Volmer–Weber (island) growth mode, for our samples we see differing structures in the silver islands depending on the deposited thickness.[38] For very low thicknesses, small, isolated, spheroidal metal particles are formed on the substrate. For higher thicknesses, the metal particles coalesce into islands of irregular shapes. At even higher thicknesses, a continuous path is formed through the silver island; this point is called the percolation threshold and is an important transition point in the electromagnetic response of the MDC film. For our silver-on-glass films, the percolation threshold occurred at a silver thickness of about 11 nm. As still more metal is deposited, the coverage fraction of metal increases until the metal completely covers the sample surface; this usually occurred for layers about 20-nm thick in our studies.

In Fig. 2 we show representative SEM images and far-field transmittance, reflectance, and absorptance data are shown for the two types of samples used in this work. The samples are labeled A and B and are fabricated with the same total metal volume fraction and the same total thickness. The mass average thicknesses of each layer in the samples are shown in Table 1. The far-field transmittance (T) and reflectance (R) spectra were measured for these samples with a commercial UV/Vis/NIR spectrophotometer (PerkinElmer Lambda950) fitted with a 150-mm integrating sphere accessory. For the reflectance measurements the sample was placed at the back side port of the integrating sphere an 8-deg angle to the incident beam.[39] The measured diffuse scattering is negligible for our samples. Absorptance was then calculated as $A = 1 - T - R$. Clearly, the samples respond quite differently to incident light, and their nanostructures are also quite distinct. For relatively thick silver layer, the metal covers most of the sample surface and forms continuous layers with a few voids (Sample A). With this type of metal layer, we obtain a 3D sample that is essentially a multilayered stack of metal layers sandwiched between dielectric layers (Sample A); this is shown schematically in Fig. 3. For thinner silver layers, the

Table 1 Mass thicknesses for each fabricated layer and thicknesses of each simulated layer for Samples A and B. The Ag metal layers are semicontinuous metal-dielectric layers, and the SiO_2 layers are pure silica.

Fabricated Thicknesses (nm)		Simulated Thicknesses (nm)			
Sample A	**Sample B**	**Sample A**	**Sample A**	**Sample B**	**Sample B**
	5.0 SiO_2				5 SiO_2
	6 Ag				6 Ag
	2.7 SiO_2				3 SiO_2
	6 Ag				6 Ag
6.6 SiO_2	2.7 SiO_2	6 SiO_2	4 SiO_2		3 SiO_2
12 Ag	6 Ag	12 Ag	14 Ag	10 Ag	6 Ag
6.6 SiO_2	2.7 SiO_2	6 SiO_2	4 SiO_2	10 Ag	3 SiO_2
12 Ag	6 Ag	12 Ag	14 Ag	10 Ag	6 Ag
10 SiO_2	7.7 SiO_2	10 SiO_2	10 SiO_2	10 Ag	8 SiO_2
Glass Substrate	Glass Substrate	Glass Substrate	Glass Substrate	Glass Substrate	Glass Substrate

metal remains in the form of disconnected islands, and no real layered structure is discernible (Sample B). This fabrication is shown schematically in Fig. 4, and tilt-view SEMs of one such film are shown in Fig. 5.

Our fabrication method can produce a structure with a great number of spheroidal metal particles with sizes of only about 5 to 10 nm. By alternating thin metal and thin dielectric layers, we create a true mixture of metal particles randomly positioned in a dielectric host. By varying the relative thicknesses of the metal and dielectric layers, a desired volume filling fraction can be achieved for 3D films. Continuing the layering fabrication process, we can produce films with arbitrary overall thicknesses. In our experiments, we have restricted our films to thicknesses of about 40 nm. However, arbitrarily thick samples can be made with this method — at the cost of rather long fabrication times. Using this layering technique, we can also produce MDC films with very high metal filling fractions that are still below percolation. This cannot be done with our usual 2D (single-metal-layer) films, as the metal coalesces together and starts to form continuous, uniform layers for high filling fractions. The ability to produce high-filling-fraction, 3D films that are near-percolation is a particularly attractive feature of our technique.

This multistep layering method is qualitatively similar to the layer-by-layer fabrication of silver-polymer composites,[41–44] although in this case we have the benefit of working in vacuum conditions and with high-purity materials without the use of binding or linking agents. We also note that this technique can produce films similar to cermets created through co-deposition by RF sputtering,[1–4] but again our method gives more flexibility because each layer can be individually adjusted during the fabrication process.

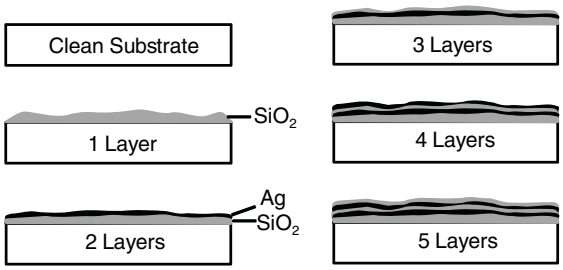

Fig. 3 Fabrication schematic for Sample A, a multilayer silver-silica composite with 2 metal layers and 3 dielectric layers. The metal and dielectric layers are clearly distinguishable, meaning this is essentially a 2D scenario for our FDTD simulations.

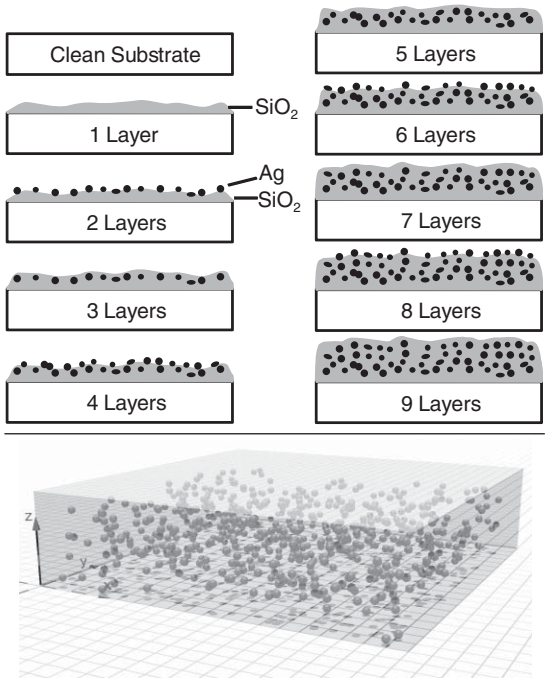

Fig. 4 Fabrication schematic for Sample B. Upper panel: Multistep layering procedure for fabricating random, 3D MDC films with controllable parameters. The final film is clearly 3D and must be simulated as such. Lower panel: Schematic image of metal particles embedded in a dielectric host and showing the 3D nature of our random MDC films [generated with persistence of view raytracer (POV-Ray) (Ref. 40)].

2.3 3D Footprinting Method and FDTD Simulations

In order to study our 3D composite films with numerical simulations, we have extended our 2D footprinting method for obtaining realistic FDTD geometries. Our first attempt at simulating 3D films was a direct extension of our previously published 2D method. In this case we obtained SEM images of the 3D film surface and, after binarization, we simply stacked the images into a layered structure. The thickness of each layer was obtained from fabrication data. This method was quite successful, but only for films that were multilayered in structure rather than

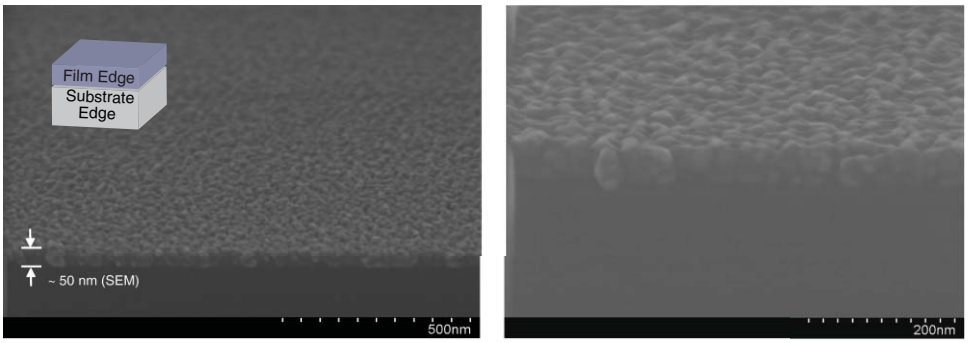

Fig. 5 A 3D composite film fabricated by the described multistep layering method on a silicon substrate. The SEM images show a tilted view of a cleaved edge of the film. Silver grains are visible throughout the film depth, indicating that the sample is an isotropic, random film. Left panel: Tilt-view SEM and inset schematic. Right panel: High-magnification image of the same sample edge.

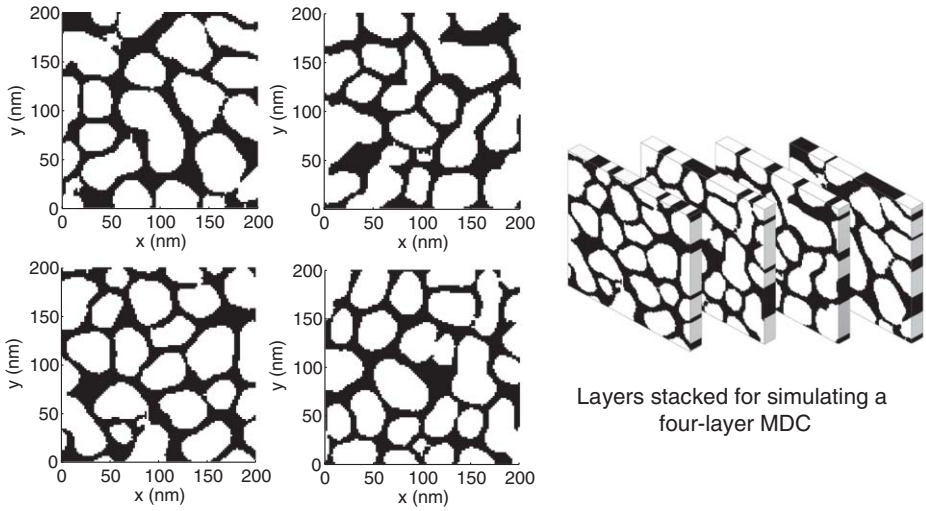

Fig. 6 Left panel: SEM image sections from our simulation for Sample B (white is silver, black is silica). Each image is 100 × 100 pixels, and the physical lengths are as shown. Right panel: Schematic showing a 4-metal-layer MDC geometry stacked for FDTD analysis. The distance between the semicontinuous metal layers has been exaggerated to show the nanostructure in each layer.

true 3D composites. We found that the binarization of the images for true 3D composite films was inaccurate because the SEM images of the sample revealed metal nanoparticles at various depths within the silica matrix. As there was no way to distinguish the uppermost particles from those deeper in the structure, we obtained black and white SEM image sections that were not representative of the sample's true nanostructure. To overcome this issue, we revised our simulation method.

In our revised 3D simulation process, we first obtained representative SEM images from the 3D sample as well as from various 2D semicontinuous films with different metal mass average thicknesses (and hence various metal particle sizes). We then compared the 2D images to the 3D image in terms of particle shape and size distributions. We selected a 2D image that corresponds to the general particle sizes and shapes seen in the 3D image. In addition, since the 3D sample was fabricated with a metal volume fraction of 65%, we selected a 2D image with a metal coverage ratio of about the same value (the chosen 2D image is shown in Fig. 1 and has a coverage ratio of 66.8%). We note that the mass average thickness of the metal layer in this case is approximately the same as the mass average thickness of each metal layer in our 3D MDC fabrication procedure. After selecting an appropriate 2D image, we composed a layered geometry of 2D film sections in order to build up a model of the 3D structure (see Fig. 6). In doing this, we duplicated the metal volume filling fraction of the real, fabricated 3D film by choosing 2D footprints from appropriate single-layer samples. We then fed this stacked structure into the FDTD solver to obtain the full electromagnetic response of the system.

Our goal in the FDTD simulations was to obtain the far-field transmittance, reflectance and absorptance spectra for the MDC, and verify our results against the experimentally measured spectra in the 300 to 2400 nm wavelength range. Both Samples A and B are about 47 nm thick with 65% metal volume filling factor and are fabricated on glass substrates that are assumed to be lossless with a refractive index $n = 1.52$. The fabricated mass average thickness of each layer is shown on the left side of Table 1. In Table 1 and in all of our discussions in this paper, the Ag metal layers are actually semicontinuous metal-dielectric layers, while the SiO_2 layers are pure silica. The initial cell sizes were chosen to be 2 nm for Sample A and 1 nm for Sample B, and due to cell discretization round-off, the simulated thicknesses are slightly different than the as-fabricated values (Table 1, right side).

The complete, binary image of each film was divided into individual frames and stacked as indicated on the right side of Table 1 (see also Fig. 1). The computational domain was 100 cells in both the x and y directions (the z direction is normal to the substrate surface), meaning that for the SEM image magnification used here, the image sections were 200 nm × 200 nm in real area for Sample A and 100 nm × 100 nm for Sample B. The simulation domain was 4000 nm in the z direction; to ensure the stability of our FDTD scheme a normalized Courant stability number of $S_{\text{norm}} = 0.5$ (Ref. 29) was taken. Thus, the time step is defined by the formula $\Delta t = S_{\text{norm}}\,\Delta/(c\sqrt{3})$, where Δ denotes the length of the edge of our uniform cubic cell. We used a perfectly-matched layer to terminate the FDTD domain in the z direction, and periodic boundary condition were applied to all other sides parallel to the z direction. The time step was about 1.926×10^{-18} s for Sample A with a total duration of 16,384 simulation steps, and for Sample B we used a time step of 9.629×10^{-19} s with a total duration of 32,768 simulation steps. Both durations were tested to be long enough to contain all the time domain information.

In order to effectively cover the broad wavelength range measured experimentally for these samples, we used two spectrally overlapping Gaussian pulses. The expression for the electric field of these pulses in the time domain is given by

$$E(t) = e^{-(t-t_0)^2/\tau^2}\sin(\omega t), \tag{1}$$

where $\omega = 2\pi c/\lambda$, $t_0 = 3T$, and $\tau = T$, ($T = 1 \times 10^{-15}$ s). The spectra of the pulses can be obtained by Fourier transforming Eq. (1), which gives Eq. (2). The Gaussian pulses have carrier frequencies corresponding to wavelengths of $\lambda_0 = 300$ nm and 1000 nm. The resulting frequency-domain spectra are plotted in Fig. 7.

$$I(\lambda) = \frac{\tau}{2}\sqrt{\pi}\,e^{-\tau^2\pi^2c^2(1/\lambda - 1/\lambda_0)^2} \tag{2}$$

Because the Gaussian pulse itself has a bandwidth that is larger than 300 THz (corresponding to a wavelength of 1000 nm), when the carrier wavelength is 1000 nm the whole spectrum extends well beyond our wavelength range of interest. In this way we can effectively cover both the short-wavelength regime (centered at 300 nm) and the long-wavelength regime in order to obtain the response of the film over the whole spectrum from 300 to 2400 nm. The dispersion properties of silver were modeled using the Drude model and were implemented through a generalized dispersion material model.[33] A piece-wise constant recursive convolution technique (PCRC2, see, for example, Ref. 45) was used to ensure second-order accuracy of the entire scheme. The Drude–Lorentz model for silver with three Lorentzian oscillator terms is

$$\varepsilon(\omega) = \varepsilon_\infty - \frac{\omega_{\text{D}}^2}{\omega^2 + i\omega\Gamma_{\text{D}}} + \sum_{m=1}^{3}\frac{f_{\text{L}m}\omega_{\text{L}m}^2}{\omega_{\text{L}m}^2 - \omega^2 - i\omega\Gamma_{\text{L}m}}, \tag{3}$$

where $\varepsilon_\infty = 2.3846$, and the remaining parameters of the model are as given in Table 2.

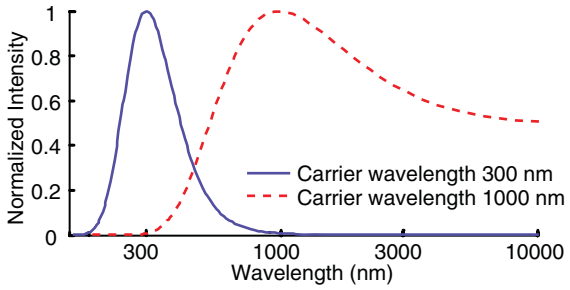

Fig. 7 Two Gaussian pulses centered at different wavelengths were used as input pulses for the FDTD simulations of the MDC films. The overlapping pulses in total cover the wavelength range of interest from 300 to 2400 nm.

Table 2 Parameters of the Drude–Lorentz dispersion model for silver.

Drude term			
ω_D (eV)		Γ_D (eV)	
9.2072		0.0210	
Lorentz terms			
m	f_{Lm}	ω_{Lm} (eV)	Γ_{Lm} (eV)
1	0.3102	4.4074	0.5221
2	0.5028	5.1476	1.0654
3	0.7393	6.4570	1.8989

The simulation was carried out on the parallel computing cluster Coates-A managed by the Rosen Center for Advanced Computing at Purdue University. The cluster consists of 640 nodes, each with two 2.5 GHz Quad-Core AMD 2380 processors. The cluster has a distributed-memory architecture with 32 GB of memory and 500 GB of disk space for each node. These nodes are connected via 10 Gigabit Ethernet and use the Red Hat Linux 5.5 operating system. The parallel-computing code is based on the domain-decomposition method.[31] For our simulations the 32 GB of memory per node can simulate a domain of about 150 × 150 × 5500 cells, which is larger than our domain for either Sample A or Sample B. Our focus in implementing a parallelized computation was to calculate the response from many different statistical realizations of the sample rather than to perform domain or spectral decomposition. A typical calculation for one realization of Sample A required 82.5 h of simulation time while for Sample B it required 371.1 h due to a finer spatial discretization and twice the number of simulation steps.

The total-scattered field separation method is used to introduce the incident source into the simulation domain.[29] The field probes, which are located close to the source side and the shade side of the domain along the propagation direction (the *z* direction), record the averaged reflected and transmitted electrical field of each frame. These results are then post-processed to obtain the numerical far-field reflection and transmission spectra. The spectra from one realization to the next change widely due to differences in the local geometry; hence the macroscopic, far-field spectral responses were obtained by averaging the results from a statistically sound number of iterations (statistical realizations) of individual spectra. In this method, we have found that approximately 20 iterations are sufficient for good agreement with our experimental data, but

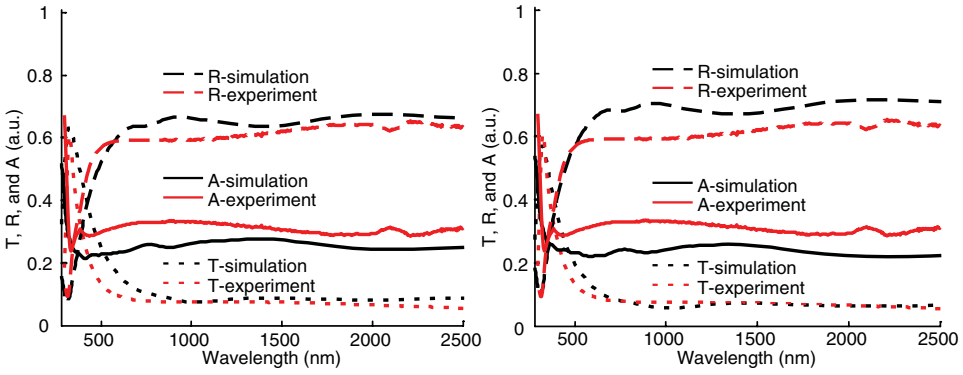

Fig. 8 Experimental and simulated far-field transmittance (*T*), reflectance (*R*) and absorptance (*A*) spectra for Sample A (silver-silica composite, 65% metal filling fraction, 47-nm thickness, 2 metal layers). In the simulations, the spectra from each of 24 geometrical realizations have been averaged to obtain the presented values. The left panel is a simulation with 12 nm Ag/6 nm SiO_2 pairs based on mass-average thicknesses, and the right panel is a revised simulation with the layer thicknesses adjusted to give a more accurate volume fraction (46-nm total thickness with two 14 nm Ag/4 nm SiO_2 pairs and about 63.6% metal volume fraction).

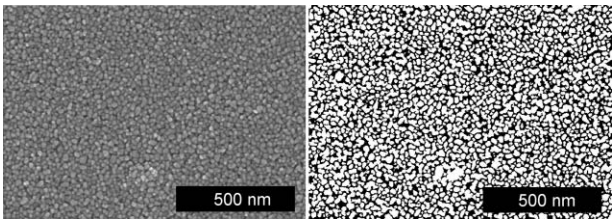

Fig. 9 SEM image of Sample B (left panel) and black/white footprint image with an adjusted threshold level so that the coverage corresponds to the experimental metal volume fraction (right panel).

we actually calculate a larger number of realizations for each sample. For Sample A (see spectra in Fig. 8) we used 48 iterations (all derived from a single SEM image), and for Sample B (see SEM image and footprint in Fig. 9 and spectra in Fig. 10) we used 24 iterations. The difference in the number of iterations is related to the fact that Sample B has twice the number of metallic layers than Sample A, and our automated process for simulating the films uses the entire SEM image to generate layers for the stacked simulation geometry.

3 Results and Discussion

Our simulation results for Samples A and B are shown in Figs. 8 and 10, respectively. We see a strong, quantitative correspondence between the simulation results and the experimental far-field spectra for both samples. This indicates that our simulation procedure is suitable for both a layered, 2D-type structure such as Sample A as well as a true 3D MDC such as Sample B. In addition, we see that the full-wave simulations with the footprint geometry accurately predict the far-field optical responses of these films, which is not possible with simpler methods like EMT.[28] Moreover, we note that our simulations accurately predict the spectral features related to interband transitions in the metal. Interband transitions in silver cause a rather sharp change in the spectral response of the films in the short-wavelength edge of the spectral range shown in Fig. 8. In our simulations, interband contributions are described by the Lorentz terms in Eq. (3)

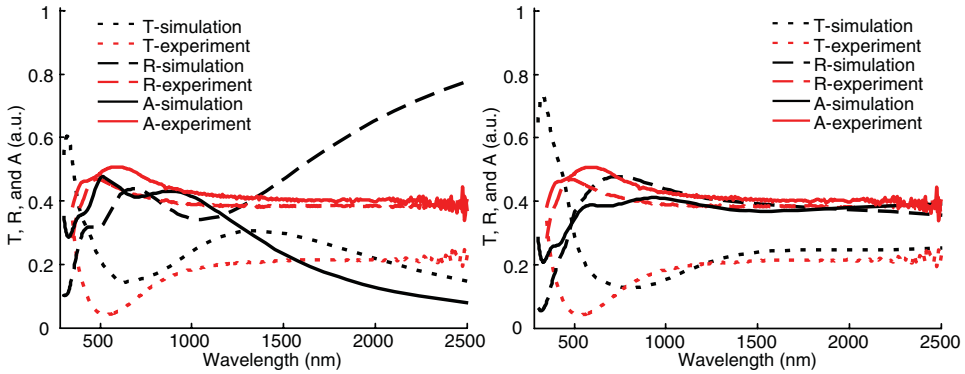

Fig. 10 Experimental and simulated far-field transmittance (T), reflectance (R), and absorptance (A) spectra for Sample B (silver-silica composite, 65% metal filling fraction, 47-nm thickness, 4 metal layers). In the simulations, the spectra from each of 24 geometrical realizations have been averaged to obtain the presented values. Left panel: Simulation with four 10-nm Ag layers adjusted to match the experimental metal volume fraction. No insulating SiO_2 layers were used in this case. Right panel: Revised simulation with layer thicknesses adjusted to match the experimental mass thicknesses (46-nm total thickness with four pairs of 6 nm Ag/3 nm SiO_2 layers and about 60% metal volume fraction for each metal layer).

for the silver permittivity, which in turn is in good correspondence with the experimental data by Johnson and Christy.[34]

In Fig. 8 we show the experimental and simulated far-field transmittance, reflectance and absorptance spectra for Sample A, which is a silver-silica composite with a 65% metal filling fraction and a total thickness of 47 nm (2 metal layers, 3 dielectric layers). For this sample, the first simulation geometry (Fig. 8, left panel) consisted of two pairs of silver/silica layers (12 nm Ag/6 nm SiO_2) and a single silica sublayer. These thicknesses were based on the mass-average thicknesses of the fabricated film. Each silver layer is modeled as a semicontinuous film, so the thicknesses listed here are the thicknesses of each metal particle in the semicontinuous film structure (we assumed vertical sidewalls for the silver grains). The right panel of Fig. 8 shows the results of a revised simulation with the layer thicknesses adjusted to give a more accurate volume fraction. In this case, the total thickness was 46 nm with two 14 nm/4 nm Ag/SiO_2 pairs and a metal volume fraction of about 63.6%. For both schemes, the simulated spectra are the average of the far-field spectra from 24 different geometrical realizations. Sample A is essentially a stacked 2D structure, and as such we expected and observed a good agreement with our experimental measurements as a result of our previous work.[30]

In Fig. 10 we show the experimental and simulated far-field transmittance spectral responses for Sample B, which is a true 3D composite structure. Sample B is also a silver-silica composite with a 65% metal filling fraction and 47-nm thickness like Sample A, but in Sample B we have 4 metal layers rather than only 2. Again we have two sets of simulated results. The left panel of Fig. 10 shows the simulated spectra for a structure with four 10-nm Ag layers adjusted to match the experimental metal volume fraction (65%). The right panel shows a revised simulation in which the layer thicknesses have been adjusted to match the experimental mass thicknesses (that is, a 46-nm total thickness with four pairs of 6 nm Ag/3 nm SiO2 layers and about 60% metal volume fraction for each metal layer). As before, the simulated spectra presented in Fig. 10 are the average of the spectra from each of 24 different geometrical realizations (see Fig. 6 for one such realization). We see again a good, quantitative agreement between the simulated spectra and the experimental values (right panel of Fig. 10). We note that the resonance peak of the simulated spectra is slightly redshifted with respect to the experimental peaks. This is likely due to the fact that we used vertical sidewalls in modeling our silver nanoparticles.

In left panel of Fig. 10 we see an interesting phenomenon that occurs when the insulating SiO_2 layers are neglected in the simulated realization of the MDC film. Although this simulation matches the fabricated film's silver volume fraction (65%), the calculated results show that the calculated reflectance of the film is significantly higher in the near-infrared wavelength range as compared to the experimental values. For a composite structure with such a high metal filling fraction and no insulating layers, the metal particles actually connect across the film's layers from the top of the MDC to the bottom. This causes a distinct change in the calculated spectral response of the composite, and these connected paths can be roughly represented as nanowires that tend to reflect near- to mid-infrared wavelengths. Since we do not observe this feature in our experimental measurements, we can conclude that our silver nanoparticles are on average completely coated by SiO_2 and are therefore isolated from other nanoparticles, as shown schematically in Fig. 4. The right panel of Fig. 10 shows the model, which includes isolating dielectric layers and results in much better agreement with experiment.

We also investigated how the predicted optical properties of the MDC films are influenced by differences in the distribution of sizes for the silver nanoparticles in the MDC. This was important to consider because effective medium theories such as Bruggeman's,[26] for example, predict that the optical properties of two MDC samples should be the same when the metal filling fractions and total thicknesses are the same. In reality, the particle size distribution does influence the optical properties of the films. To study this influence, we generated realizations of stacked layers corresponding to Sample B (which was fabricated with a 47-nm thickness, four metal layers, and a 65% metal filling fraction) using two different particle distributions. We derived the particle distributions from SEM images from two different samples. One SEM image was from the actual Sample B film, and the other was from Sample C, which was a

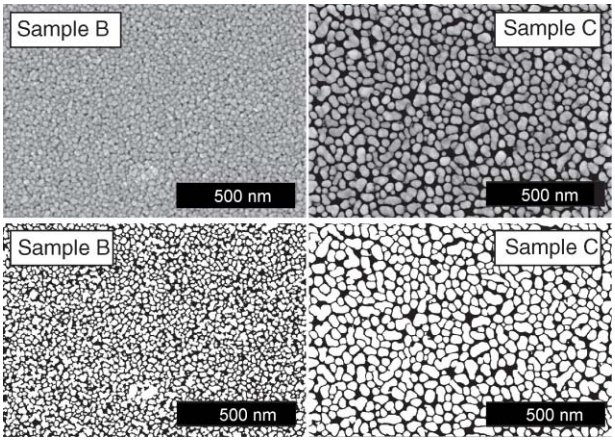

Fig. 11 SEM images (top) and binary images (bottom) of Sample B (left) and a single-layer semicontinuous metal film (Sample C, right). The mass thickness of Sample C is the same as one of the metal layers of Sample B. The images have different particle size distributions, which lead to changes in their calculated spectral responses.

single-metal-layer silver/silica semicontinuous film whose metal coverage was chosen to be the same as a metal layer of Sample B. These SEM images and their binary counterparts are shown in Fig. 11. The particle area distributions of the binary images are as defined in Eq. (4)

$$P_i = N_i / N_{\mathrm{TOT}}, \tag{4}$$

where N_i is the number of particles within the range $[i, i+\Delta)$, the step size Δ is chosen to be 1 nm^2, and N_{TOT} is the total number of particles. Hence P_i represents the percentage of particles within a given area range, and plotting P_i versus particle area gives us the histogram of the binary image, as shown in Fig. 12.

The particle area distributions are clearly different, with a larger average particle area for the Sample C distribution. From the binary images, we generated geometrical realizations corresponding to Sample B and calculated the expected far-field spectral responses. The simulation parameters were the same as those of the right panel of Fig. 10 (i.e., we used the Drude–Lorentz model for the silver permittivity and four pairs of 6 nm Ag/3nm SiO_2 layers, and the simulation domain and time steps were as noted for Sample B above). Therefore, the only differences between the two realizations are related to their particle size distributions. The averaged, far-field spectral responses of these two realizations are shown in Fig. 13. In the left panel we show

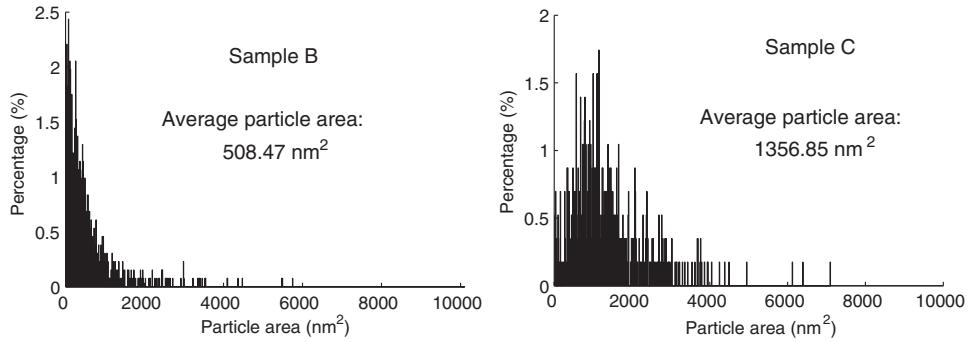

Fig. 12 Particle size distributions from the binary images of Fig. 11. Average particle areas are as indicated. The distributions are clearly different, which leads to different far-field spectral responses for the MDC films.

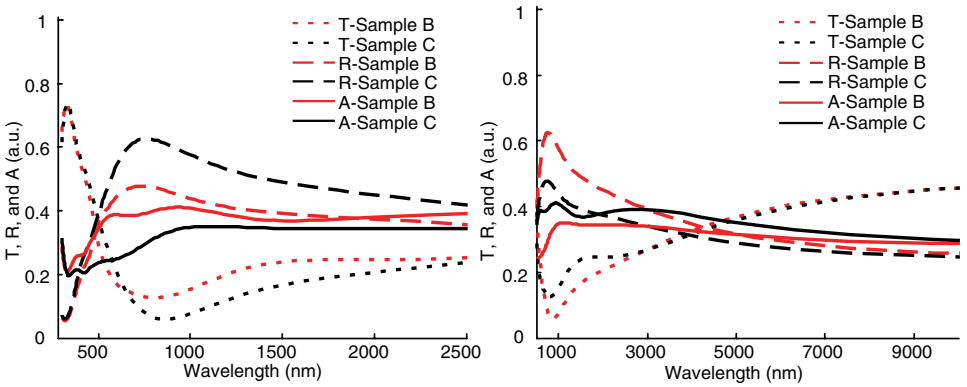

Fig. 13 The simulation results for transmittance (T), reflectance (R), and absorptance (A) spectra for Sample B using four pairs of 6 nm Ag/3 nm SiO_2 layers and the two different particle distributions of Fig. 12. Left panel: Calculation results for UV, visible, and near-infrared wavelengths. Right panel: Calculation results extending into the mid-infrared range. The results from the different particle distributions converge for very short wavelengths around 300 nm and for longer wavelengths into the mid-infrared range, while at visible and near-infrared wavelengths the discrepancies between the distributions are clearly evident.

the UV, visible, and near-infrared responses of the films, and in the right panel we show the responses for longer wavelengths into the mid-infrared range. It is interesting that the T/R/A spectral results match for the two distributions in the short-wavelength range from about 300 to 600 nm, and they also match in the long-wavelength range beyond about 7000 nm, which is clearly seen in the right panel of the Fig. 13. However, we see that differences in the particle size distributions significantly affect the results in the part of the visible and near-infrared wavelength ranges. These results support our assertion that effective medium theories are not sufficient for predicting the optical response of MDCs, particularly when the metal inclusions strongly interact.

For the long-wavelength range, the wavelengths are long enough that the silver nanoparticle shapes are not felt by the incident wave, and the material acts like a bulk, diluted metal. In the wavelengths from about 600 nm and into the near-infrared region, however, the optical response should be dominated by strongly interacting metal nanoparticles that support localized plasmon resonances and hot spots.[9–12] In this range, the localized resonance effects related to the geometry and the distribution of the particle sizes should be taken into account. It is therefore in this regime that we find discrepancies between the calculated responses from realizations made with different particle size distributions.

4 Conclusions

We have shown that inherently 3D metal-dielectric films can be created using a multistep, layered deposition process. These films are comparable in composition to a co-deposited MDC, but in our method there is more control over the details of the structure such as the particle size distribution, volume fraction, and interparticle spacing, in addition to high reproducibility. We have described the details of this fabrication method and used it to make a number of MDC samples, which were then characterized optically. These samples are not sufficiently described by effective medium theory modeling, and as a result we have also turned our attention to simulating random MDCs using more accurate simulations such as FDTD.

We have developed a method to obtain realistic geometries of fabricated 3D MDC samples. Our simulation method, which we call footprinting in reference to the 2D method on which it is based, is used to obtain geometries consistent with our fabricated samples and allow us to perform full-wave FDTD simulations of the sample nanostructure. We obtained the detailed near- and

far-field electromagnetic responses of model MDC structures and averaged the responses over a number of realizations, recreating the macroscopic response of the real sample. Comparing our results with the experimentally measured far-field spectra of the actual samples, we found good agreement between the simulated and experimental results, even when a relatively small number of geometrical realizations were used. Our simulation results support the observation that the resonance phenomena in the MDC are influenced by the layer structure of the film as well as other features of the composite, and not solely by the volume filling fraction and constituent permittivities, as would be predicted by effective medium theories. In particular, the particle size distribution influences the spectral response of the film, and our results indicate that this influence is strong in the visible and near-infrared wavelength range.

Our fabrication and simulation methods and our results can be applied to other random MDC and cermet structures where well-controlled fabrication and detailed, full-wave simulations are often difficult or impossible to obtain. We expect our approach will be useful in studying complex, random geometries whose properties cannot be adequately described by mean-field theories like Bruggeman's effective medium theory. Going forward, we intend to use this simulation methodology in projects related to near-field enhancement, obscurants and filters, and fundamental studies on plasmonic materials.

Acknowledgments

This work was funded in part by the U.S. Army Research Office Grant Nos. 50372-CH-MUR and W911NF-07-D-001, and by a graduate fellowship sponsored by Sandia National Laboratory.

References

1. C. Sella, S. Chernot, V. Reillon, and S. Berthier, "Influence of the deposition conditions on the optical absorption of Ag-SiO_2 nanocermet thin films," *Thin Solid Films* **517**, 5848–5854 (2009).
2. P. Reinhardt, C. Reinhardt, G. Reisse, and C. Weissmantel, "Electrical and structural properties of ion beam sputtered silver-SiO_2 cermet films," *Thin Solid Films* **51**, 99–104 (1978).
3. C. Sella, A. Bichri, J. C. Martin, J. Lafait, K. Driss-Khodja, and S. Berthier, "Adjustable optical properties of coatings based on cermet thin films near the percolation threshold," *Phys. A* **157**, 555–560 (1989).
4. M. Gadenne, P. Gadenne, J. C. Martin, and C. Sella, "Composition and electrical properties of Au-$A1_2O_3$ cermet thin films: A critical study," *Thin Solid Films* **221**, 183–190 (1992).
5. V. M. Shalaev, M. I. Stockman, and R. Botet, "Resonant excitations and nonlinear optics of fractals," *Phys A* **185**, 181–186 (1992).
6. V. P. Drachev, W. D. Bragg, V. A. Podolskiy, V. P. Safonov, W. T. Kim, Z. C. Ying, R. L. Armstrong, and V. M. Shalaev, "Large local optical activity in fractal aggregates of nanoparticles," *J. Opt. Soc. Am. B* **18**, 1896–1903 (2001).
7. A. K. Sarychev, R. C. McPhedran, and V. M. Shalaev, "Electrodynamics of metal-dielectric composites and electromagnetic crystals," *Phys. Rev. B* **62**, 8531–8539 (2000).
8. V. A. Podolskiy, A. K. Sarychev, E. E. Narimanov, and V. M. Shalaev, "Resonant light interaction with plasmonic nanowire systems," *J. Opt. A. Pure Appl. Opt.* **7**, S32–S37 (2005).
9. A. K. Sarychev and V. M. Shalaev, "Electromagnetic field fluctuations and optical nonlinearities in metal-dielectric composites," *Phys. Rep.* **335**, 276–371 (2000).
10. D. A. Genov, A. K. Sarychev, and V. M. Shalaev, "Plasmon localization and local field distribution in metal-dielectric films," *Phys. Rev. E* **67**, 056611 (2003).
11. S. Ducourtieux, V. A. Podolskiy, S. Grésillon, S. Buil, B. Berini, P. Gadenne, A. C. Boccara, J. C. Rivoal, W. D. Bragg, K. Banerjee, V. P. Safonov, V. P. Drachev, Z. C. Ying, A. K.

Sarychev, and Vladimir M. Shalaev, "Near-field optical studies of semicontinuous metal films," *Phys. Rev. B* **64**, 165403 (2001).
12. S. Ducourtieux, S. Gresillon, A. C. Boccara, J. C. Rivoal, X. Quelin, P. Gadenne, V. P. Drachev, W. D. Bragg, V. P. Safanov, V. P. Podolskiy, Z. C. Ying, R. L. Armstrong, and V. M. Shalaev, "Percolation and fractal composites: Optical studies," *J. Nonlinear Opt. Phys. Mater.* **9**(1), 105–116 (2000).
13. M. Moskovits, "Surface-enhanced spectroscopy," *Rev. Mod. Phys.* **57**, 783–826 (1985).
14. V. P. Drachev, M. D. Thoreson, E. N. Khaliullin, V. J. Davisson, and V. M. Shalaev, "Surface-enhanced Raman difference between human insulin and insulin lispro detected with adaptive nanostructures," *J. Phys. Chem. B* **108**, 18046–18052 (2004).
15. V. P. Drachev, M. D. Thoreson, V. Nashine, E. N. Khaliullin, D. Ben-Amotz, V. J. Davisson, and V. M. Shalaev, "Adaptive silver films for surface-enhanced Raman spectroscopy of biomolecules," *J. Raman Spectrosc.* **36**, 648–656 (2005).
16. V. P. Drachev, V. C. Nashine, M. D. Thoreson, D. Ben-Amotz, V. J. Davisson, and V. M. Shalaev, "Adaptive silver films for detection of antibody-antigen binding," *Langmuir* **21**, 8368–8373 (2005).
17. K. Kneipp, Y. Wang, H. Kneipp, L. T. Perelman, I. Itzkan, R. R. Dasari, and M. S. Feld, "Single molecule detection using surface-enhanced Raman scattering (SERS)," *Phys. Rev. Lett.* **78**, 1667–1670 (1997).
18. M. Osawa and M. Ikeda, "Surface-enhanced infrared absorption of p-nitrobenzoic acid deposited on silver island films: Contributions of electromagnetic and chemical mechanisms," *J. Phys. Chem.* **95**, 9914–9919 (1991).
19. A. Hartstein, J. R. Kirtley, and J. C. Tsang, "Enhancement of the infrared absorption from molecular monolayers with thin metal overlayers," *Phys. Rev. Lett.* **45**, 201–204 (1980).
20. M. Osawa, "Surface-enhanced infrared absorption," *Top. Appl. Phys.* **81**, 163–182 (2001).
21. D. Enders and A. Pucci, "Surface enhanced infrared absorption of octadecanethiol on wet-chemically prepared Au nanoparticle films," *Appl. Phys. Lett.* **88**, 184104 (2006).
22. M. Westphalen, U. Kreibig, J. Rostalski, H. Lüth, and D. Meissner, "Metal cluster enhanced organic solar cells," *Sol. Energy Mater. Sol. Cells* **61**, 97–105 (2000).
23. A. Yakimov and S. R. Forrest, "High photovoltage multiple-heterojunction organic solar cells incorporating interfacial metallic nanoclusters," *Appl. Phys. Lett.* **80**, 1667–1670 (2002).
24. D. A. Genov, A. K. Sarychev, and V. M. Shalaev, "Metal-dielectric composite filters with controlled spectral windows of transparency," *J. Nonlinear Opt. Phys. Mater.* **12**(4), 419–440 (2003).
25. P. Nyga, V. P. Drachev, M. D. Thoreson, and V. M. Shalaev, "Mid-IR plasmonics and photomodification with Ag films," *Appl. Phys. B* **93**, 59–68 (2008).
26. D. A. G. Bruggeman, "Calculation of various physical constants of heterogeneous substances. I. dielectric constants and conductivity of mixed bodies from isotropic substances," *Ann. Phys.* **24**, 636–679 (1935) (in German).
27. P. Sheng, "Theory of the dielectric function of granular composite media," *Phys. Rev. Lett.* **45**, 60–63 (1980).
28. R. B. Nielsen, M. D. Thoreson, W. Chen, A. Kristensen, J. M. Hvam, A. Boltasseva, and V. M. Shalaev, "Toward superlensing with metal-dielectric composites and multilayers," *Appl. Phys. B* **100**, 93–100 (2010).
29. A. Taflove and S. C. Hagness, *Computational Electromagnetics: The Finite Difference Time Domain Method* (Artech House, Norwood, Massachusetts, 2000).
30. U. K. Chettiar, P. Nyga, M. D. Thoreson, A. V. Kildishev, V. P. Drachev, and V. M. Shalaev, "FDTD modeling of realistic semicontinuous metal films," *Appl. Phys. B* **100**, 159–168 (2010).

31. A. V. Kildishev, U. Chettiar, and V. M. Shalaev, "Simulation of optical negative index materials using parallel FDTD method," *Proceedings of the 22nd Annual Review of Progress in Applied Computational Electromagnetics*, ACES, Miami, FL (2006).
32. T. Grosges, A. Vial, and D. Barchiesi, "Models of near-field spectroscopic studies: comparison between finite-element and finite-difference methods," *Opt. Express* **13**(21), 8483–8497 (2005).
33. L. J. Prokopeva, J. Borneman, and A. V. Kildishev, "Optical dispersion models for time-domain modeling of metal-dielectric nanostructures," *IEEE Trans. Magn.* **47**(5), 1150–1153 (2011).
34. P. B. Johnson and R. W. Christy, "Optical constants of the noble metals," *Phys. Rev. B* **6**, 4370–4379 (1972).
35. V. P. Drachev, U. K. Chettiar, A. V. Kildishev, H. K. Yuan, W. Cai, and V. M. Shalaev, "The Ag dielectric function in plasmonic metamaterials," *Opt. Express* **16**, 1186–1195 (2008).
36. K. P. Chen, V. P. Drachev, J. D. Borneman, A. V. Kildishev, and V. M. Shalaev, "Drude relaxation rate in grained gold nanoantennas," *Nano Lett.* **10**, 916–922 (2010).
37. T. J. Miller, "Monitoring TOC in UPW at the Birck Nanotechnology Center," *Ultrapure Water-Micro*, Phoenix, AZ (2010).
38. M. Ohring, *Materials Science of Thin Films: Deposition and Structure*, Academic Press, San Diego, (2001); J. A. Venables, G. D. T. Spiller, and M. Hanbucken, "Nucleation and growth of thin films," *Rep. Prog. Phys.* **47**, 399–459 (1984).
39. S. L. Storm, A. Springsteen, and T. M. Ricker, "The use of center mount sample holders in reflectance spectroscopy," Labsphere Application Note No. 02 (1998).
40. Persistence of Vision^{TM} Raytracer (Version 3.62), Persistence of Vision Pty. Ltd., Williamstown, Victoria, Australia, www.povray.org.
41. J. Schmitt, G. Decher, W. J. Dressick, S. L. Brandow, R. E. Gee, R. Shashidhar, and J. M. Calvert, "Metal nanoparticle/polymer superlattice films: fabrication and control of layer structure," *Adv. Mater* **9**(1), 61–65 (1997).
42. J. Werner, A. Heilmann, V. Hopfe, F. Homilius, B. Steiger, and O. Stenzel, "Changes of the optical properties of plasma polymer silver composite films caused by laser-annealing," *Thin Solid Films* **237**, 193–199 (1994).
43. H. Takele, S. Jebril, T. Strunskus, V. Zaporojchenko, R. Adelung, and F. Faupel, "Tuning of electrical and structural properties of metal-polymer nanocomposite films prepared by co-evaporation technique," *Appl. Phys. A* **92**, 345–350 (2008).
44. H. Takele, H. Greve, C. Pochstein, V. Zaporojtchenko, and F. Faupel, "Plasmonic properties of Ag nanoclusters in various polymer matrices," *Nanotechnology* **17**(14), 3499–3505 (2006).
45. J. Schuster and R. Luebbers, "An accurate FDTD algorithm for dispersive media using a piecewise constant recursive convolution technique," *IEEE Antennas Propagat. Soc. Int. Symp.*, Atlanta, GA, pp. 2018–2021 (1998).

Biographies and photographs of the authors not available.